Atomic Layer Deposited Interlayers for Robust Metal–Polymer Interfaces

Johanna Byloff,[†,‡] Claus Othmar Wolfgang Trost,[¶] Vivek Devulapalli,[†] Shuhel Altaf-Hussein,[§,‖] Damien Faurie,[§] Pierre–Olivier Renault,[‖] Thomas Edward James Edwards,[†] Megan J. Cordill,[¶] Daniele Casari,[†] and Barbara Putz[*,†,⊥]

†*Empa, Swiss Federal Laboratories for Materials Science and Technology, Laboratory for Mechanics of Materials and Nanostructures, Feuerwerkerstrasse 39, Thun, 3603, Switzerland*

‡*Laboratory for Nanometallurgy, ETH Zurich, Vladimir–Prelog–Weg 5, Zurich, 8093, Switzerland*

¶*Erich Schmid Institute of Materials Science, Austrian Academy of Sciences, Jahnstraße 12, Leoben, 8700, Austria*

§*LSPM–CNRS, UPR3407, Université Sorbonne Paris Nord, 99 Avenue Jean–Baptiste Clément 93430, Villetaneuse, France*

‖*Institut Pprime, CNRS – Université de Poitiers, 86073 Poitiers Cedex, France*

⊥*Department of Materials Science, Montanuniversität Leoben, Franz Josef Straße 18, Leoben, A–8700, Austria*

E-mail: barbara.putz@empa.ch

Abstract

The development of materials for flexible electronics and space applications critically depends on the mechanical integrity of metal thin films deposited on polymer

substrates. However, film cracking and interfacial delamination at the metal–polymer interface limit performance significantly. In this work, we demonstrate enhanced adhesion and electromechanical properties of magnetron–sputtered aluminum films on polyimide substrates through the introduction of an amorphous AlO_xH_y interlayer deposited via atomic layer deposition (ALD). Employing in–situ X–ray diffraction and electrical resistance measurements during uniaxial and equi–biaxial tensile testing, we reveal that our integrated ALD–PVD approach yields an up-to-threefold increase in both the crack onset (COS) and electronic failure strains (EFS) and doubles the adhesion energy of the system. The AlO_xH_y interlayer alters interface-driven deformation mechanisms from absorbing to blocking dislocations at the interface. The strengthened metal–polymer interface, in turn, improves electromechanical stability at expanded strain ranges, resulting in shorter and more angled cracks in the metal film. This enhanced strain tolerance opens up alternative pathways for the development of flexible thin film devices that can conform to complex curved surfaces and withstand deformation while maintaining their functional properties.

Keywords

Thin Films, Electromechanical Properties, Atomic Layer Deposition, Flexible Substrates, Tensile Testing, Adhesion

1 Introduction

Metal thin films on polymer substrates are instrumental in applications ranging from flexible electronics to space technology. In the electronics industry, multilayer interconnect packaging makes use of polyimide dielectrics, with polyimide separating metal wires and vias.[1] In the space sector, Aluminum (Al)–polyimide film–substrate systems are deployed as the sun shield subsystem of the James Webb Space Telescope or as optical blocking filters for X–ray detectors on the X–ray observatory ATHENA.[2,3] Polyimide provides good interfacial adhe-

sion with Al, and high temperature resistance up to 400 °C.[4,5] Al thin films show an increase in roughness and only a slight decrease in hardness after annealing at 300°C.[6] Al-PI-based multilayer insulation systems (MLIs) currently withstand ± 150°C in low earth orbit and will face increased thermal loads on the BepiColombo spacecraft en-route to mercury due to solar proximity. As a coating material, Aluminum is also known for good conductivity, broad–band reflectivity, and low cost.[7] For the previously mentioned applications, it is crucial to conserve the functional properties of the system by maintaining mechanical integrity during use.[8] For instance, component lifetime is shortened due to mechanical failure caused by cracking in or delamination of the metal thin film.[9,10] Shortened lifetimes are problematic as space technology cannot easily be replaced, and self–healing in thin metallic films is still an emerging field of study.[11]

Adhesion is an important factor that governs thin film failure. When straining a ductile metal film deposited onto a polymer substrate, such as Al on polyimide, the film deforms plastically, as the film adheres to the substrate surface and strain localization (necking) is suppressed.[12] However, if this is no longer true because the interface adhesion is low, the ductile film locally becomes a freestanding metal film, leading to rupture at lower strains.[12] Various factors influence adhesion, including residual stress, film thickness, microstructure of the thin film and the interfacial reactions at the interface between thin film and substrate, which are often difficult to decouple from each other.[13,14] Brittle interlayers can be used to facilitate surface bonding and improve adhesion between polymer substrates and metallic thin films.[15] However, adhesion interlayers can also be detrimental to mechanical strength and damage resistance, as their brittle nature can lead to premature mechanical failure.[16] This is due to the interlayer cracking at low strains, inducing highly localized stress concentrations in the overlying film. Subsequently, the whole film system then exhibits through–thickness cracking at lower strains compared to a film system without a brittle adhesion interlayer.[17]

In the Al–polyimide system, intermixing at the interface occurs during thermal evaporation, under laboratory sputtering conditions or when polyimide is spin–coated onto alu-

minum.[18,19] In the latter case, the polyimide reacts with the native Al–oxide during curing heat treatment, while in the former case, vaporized Al atoms impinge on and react primarily with C=O bonds on the polyimide surface.[20] The resulting amorphous interlayer has a thickness of around 5 nm and is composed of an Al–O–C complex.[20] It exhibits excellent thermal stability and has been found to benefit adhesive and mechanical properties by promoting annihilation of dislocations at the interface.[18,21] In contrast to this, systems without intermixing, including Al/FEP or Al–polyimide sputtered under industrial process conditions have been associated with poor adhesive and mechanical performance, as well as limited thermal stability.[22–24] In this study, we emulate the beneficial 5 nm native interlayer by introducing an amorphous atomic layer deposited (ALD) alumina interlayer between the Al thin film and the polyimide substrate. This is done to leverage adhesion–promoting qualities while conserving the ductile nature of the interlayer and metal film. Nanometer-scale ALD coatings of alumina have been studied on various polymers, demonstrating remarkable effectiveness as gas diffusion barriers.[25] Provided a perfect structure and the absence of geometrical defects, thin amorphous ALD–oxide layers can be extremely strong and ductile, whereby the limiting factor for structural perfection are often the layer thickness or H content.[26] For ALD–alumina, the identified thickness limit for brittle cracking is above or equal to 5 nm.[27–29]

The proposed interface modification is enabled by using a unique ALD–physical vapor deposition (PVD) cluster setup with in–vacuo transfer capability. The deformation mechanisms of the resulting film–substrate couples under application–relevant loading conditions were evaluated via state of the art uni–and biaxial mechanical tensile testing with in–situ XRD and electrical resistance measurements and adhesion analysis using tensile induced deformation (TID).[30–32] Combined with quantitative chemical, microstructural and post–mortem crack analysis, we can demonstrate that ALD interface engineering significantly improves the electro–mechanical performance of our film system. This paves the way towards reliable flexible electronics or space applications and ensures high interface quality for material

combinations or fabrication methods with limited capability for intermixing reactions at the interface.

2 Results and discussion

2.1 Interface and Thin Film Microstructure

Using our novel ALD–PVD approach, Al films with and without ALD interlayer were fabricated. In the following, these systems will be referred to as "native interlayer" (no ALD) and "artifical interlayer" (5 nm ALD at the interface). The chemistry and microstructure of the different interfaces is revealed through high–angle annular dark–field scanning transmission electron microscopy (HAADF–STEM) imaging, energy–dispersive X–ray spectroscopy (EDS) maps and high resolution (HR)–TEM cross–sections (Figure 1).

Interlayer thicknesses were measured from cross–sectional HR–TEM images (Figure 1 A and B). The boundaries between the different regions are indicated with white horizontal lines. The native interlayer thickness was measured as 5.6 ± 0.9 nm, comparable to literature values.[18,29,33] Film thickness of the artificial interlayer was measured as 5.7 ± 1.5 nm, matching the projected growth–per–cycle (GPC) of 0.14 nm for ALD–alumina.[34] FFT patterns of the interlayers, shown as inlays in Figure 1, are distinctly different from Al and polyimide, and confirm both interlayers as amorphous. A narrow bright region directly underneath the ALD layer in Figure 1 B (transition region), with a finer structure than the polyimide substrate, could be related to vapor phase infiltration.[35]

From the EDS analysis in Figure 1 C (native interlayer system), the whole width of the intermixed region is measured as roughly 30 nm, significantly wider compared to the 5 nm Al–O–C complex previously reported for sputter–deposited Al.[20,29] The chemical profiles of individual elements are used to identify possible sub–regions. Notably, there is significant accumulation of O (blue peak in Figure 1 C ii) at the transition between the Al layer and the polyimide substrate, coinciding with a linear decrease of Al (grey line, Figure 1 C ii).

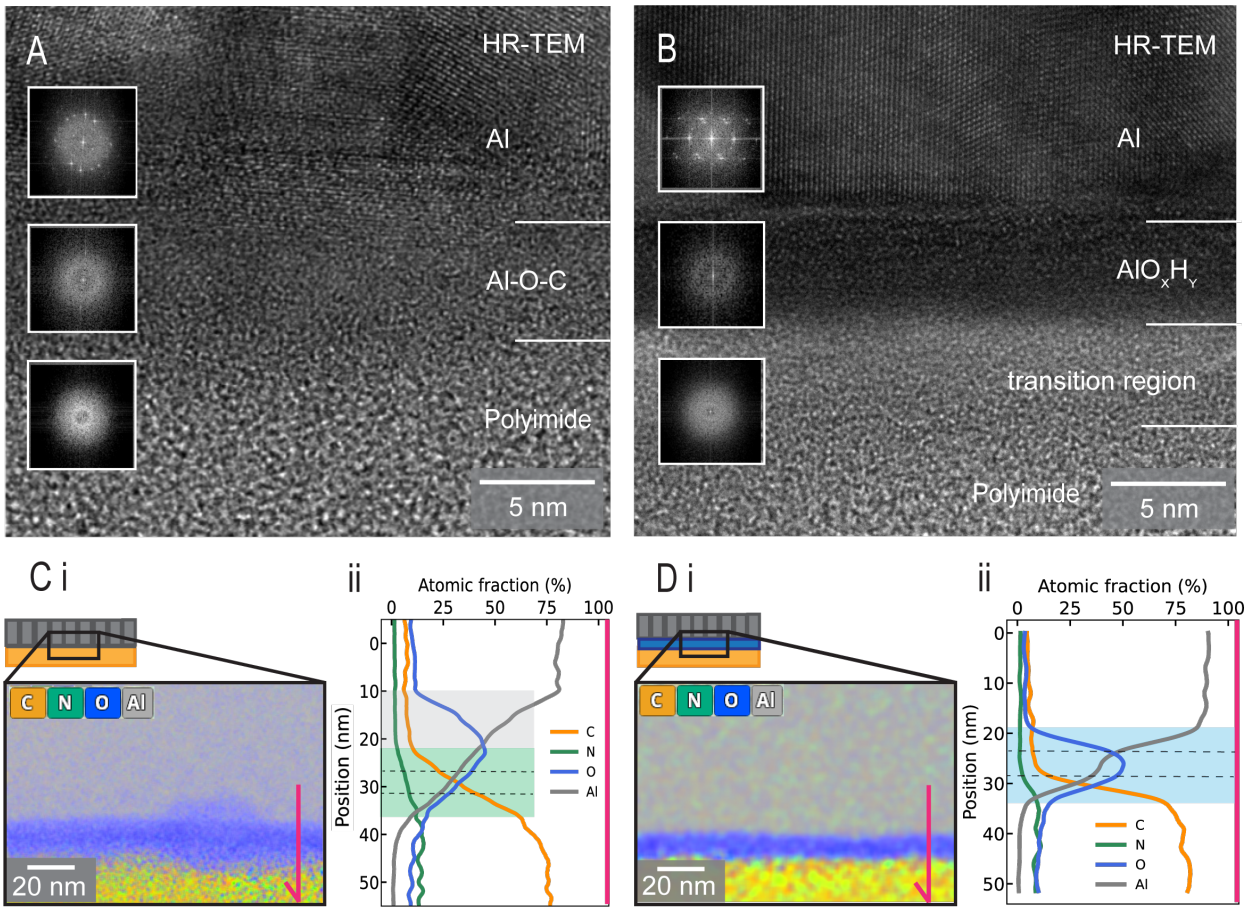

Figure 1: Cross–sectional TEM analysis of native (Al/PI) and artificial (Al/am–AlO_xH_y/PI) interlayer systems. A and B: HR–TEM cross–section of Al/PI and Al/am–AlO_xH_y/PI interlayer systems, respectively. FFT patterns are shown as square inlays to ascertain crystallinity of the respective region. C and D i: EDS map of the Al/PI and Al/am–AlO_xH_y/PI interlayer system, respectively. The diffuse blue region in the Al layer in C i is due to beam damage. C and D ii: atomic fractions (%; C, N, O, Al) of a line scan across the interface marked in pink. In both graphs, the interfacial region is underlaid in blue and grey with further explanation in the text.

In contrast, the N (green) and C (orange) signals increase only at the maximum of the O peak. As these elements can be clearly attributed to the polymer substrate, this increase defines the upper boundary for Al–O–C complex formation (native interlayer, green region in Figure 1 C ii. The apparent increased interlayer thickness in EDS measurements is due to the geometric projection of the inclined layer, where precise normal alignment is hindered by the beam–sensitive polyimide substrate. Additionally, beam–specimen interactions cause signal spreading, manifesting as a Gaussian composition profile of oxygen, as seen in Figure 1 D ii. The 10 nm transition region above the native interlayer (grey region in Figure 1 C ii) is possibly related to oxidation of the Al–O–C complex. Similar oxide formation without C has been previously observed at the Al–Polyimide interface.[24]

For the artificial ALD–interlayer system (Figure 1 D) the intermixed region at the interface is narrower, with N, C, and O exhibiting similar concentration profiles (Figure 1 D ii). Notably, the oxygen peak here coincides with a shoulder in the Al signal, confirming a stable Al and O concentration for this region, which corresponds to the 5 nm ALD–deposited interlayer (dashed lines in 1 D ii). Similarly to the native interlayer, experimental constraints result in an apparent broadening (blue area in Figure 1 D ii). In both cases, further into the polymer substrate, the measured element ratio correlates well with the nominal chemical composition of the polyimide substrate (76 at% C, 17at% O, and 7 at% N).

The elemental composition of the room–temperature (RT) deposited ALD alumina interlayer was ascertained via RBS/ERDA compositional depth analysis on 75 nm thick films. Elemental ratios of 47.5 at% O, 23.5 at% Al, and 27.5 at% H resulted in an $Al_{0.24}O_{0.48}H_{0.28}$ stoichiometry, with significantly higher amount of H than films deposited at 120 °C (ALD window of alumina).[36] Increased H content (up to 35 at%) for RT ALD is related to H atoms forming covalent –OH hydroxyl bonds with O in coordination spheres of interstitial Al cations and could influence mechanical and adhesive properties.[37]

To distinguish between the influence of interface structure (native/artificial) and thin film microstructure on electromechanical properties, films with differing Al microstructures

were investigated. Automated crystal orientation mapping (ACOM) was carried out on three representative cross–sectional Al films subsequently subjected to mechanical testing to assess grain size, orientation, and a possible influence of the ALD interlayer on the Al thin film microstructure (Figure 2 A–C).

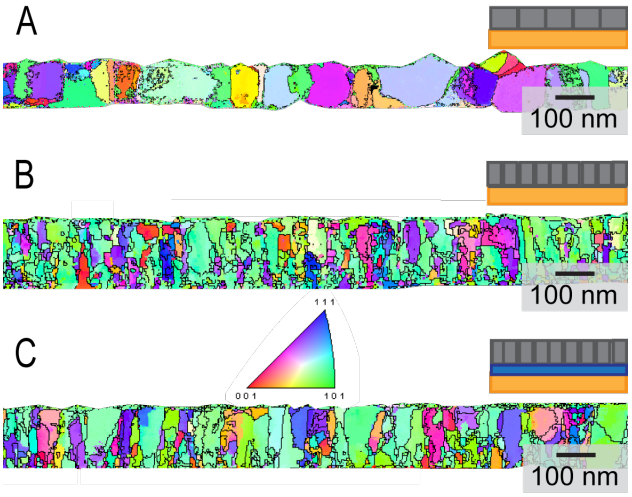

Figure 2: ACOM inverse pole figure (IPF)-z maps (out-of-plane direction) of the investigated Al microstructures. A, B: Al films on polyimide without ALD (native interlayer system). C: Al film with 5 nm am–AlO_xH_y artificial ALD interlayer on polyimide. Grain boundaries are marked with black lines. Note that only the Al layer is shown.

All Al layers have a homogeneous thickness with randomly oriented, mostly columnar, nanocrystalline grains. For two films without ALD interlayer the average grain size / layer thickness was measured as 57 ± 47 / 120 ± 11 nm (Figure 2 A) and 24 ± 11 / 172 ± 6 nm (Figure 2 B). Note that the coarser microstructure shown in Figure 2 A better resembles Al layers on polyimide previously shown in literature (grain size 91 ± 27 nm[28]). As the Al film with ALD interlayer (Figure 2 C) has an average grain size and layer thickness of 26 ± 15 / 164 ± 5 nm, we can conclude that identical Al thin film microstructures have been achieved with and without the ALD interlayer.

2.2 Electromechanical Behavior

To investigate the influence of the interface structure on electromechanical properties, uniaxial tensile tests with in–situ XRD (Al (111) Bragg peak) and electrical resistivity measurements were performed. Figure 3 A–B shows the different evolution of the axial (σ_x, black filled symbols) and transverse (σ_y, grey open symbols) Al film stress as a function of applied engineering strain ε_x with native or ALD interlayer, respectively. Mechanical deformation characteristics equivalent to fracture or yield stresses can be derived from axial measurements, while transverse measurements yield insight into buckling phenomena and provide a second correlative dataset.[16,38] Corresponding evolution of FWHM is provided as Figure S2 in the supporting information. A slight FWHM increase is noted upon reaching of the yield stress, however, the data are not conclusive due to wide error margins. No XRD signal is obtained from either the native or artificial interlayer due to their limited thickness and amorphous structure. The evolution of the normalized resistance ratio R/R_0 recorded during axial measurements in relation to the linear increase expected from constant volume approximation (orange lines in Figure 3 A–B) can aid with the determination of mechanical deformation domains. Electrical failure will be discussed in detail in a separate paragraph, considering all interface, microstructure, and loading cases.

Initially, the Al layers exhibit a neutral / slightly compressive residual stress depending on the interface structure (axial: $\sigma_{res.,nat.,uni,ax.} = 50 \pm 17$ MPa, $\sigma_{res.,art.,uni,ax.} = —258 \pm 18$ MPa; transverse: $\sigma_{res.,nat.,uni,trans.} = —48 \pm 33$ MPa, $\sigma_{res.,art.,uni,trans.} = —45 \pm 10$ MPa, green filled and unfilled symbols Figure 3). In general, compressive residual stress levels in a coating shift failure to higher applied strains, a positive effect induced by the ALD interlayer. Differences in Figure 3 A between axial and transverse residual stress measurements at the beginning of the experiment can be ascribed to pre-loading of the sample. Upon loading, the native interlayer system (Figure 3 A) shows fairly brittle deformation behavior, with a characteristic peak in the axial stress–strain curve around 2.5% applied strain (ultimate tensile strength $\sigma_{x_{max},nat.} = 562 \pm 42$ MPa), corresponding to a rapid increase in electrical

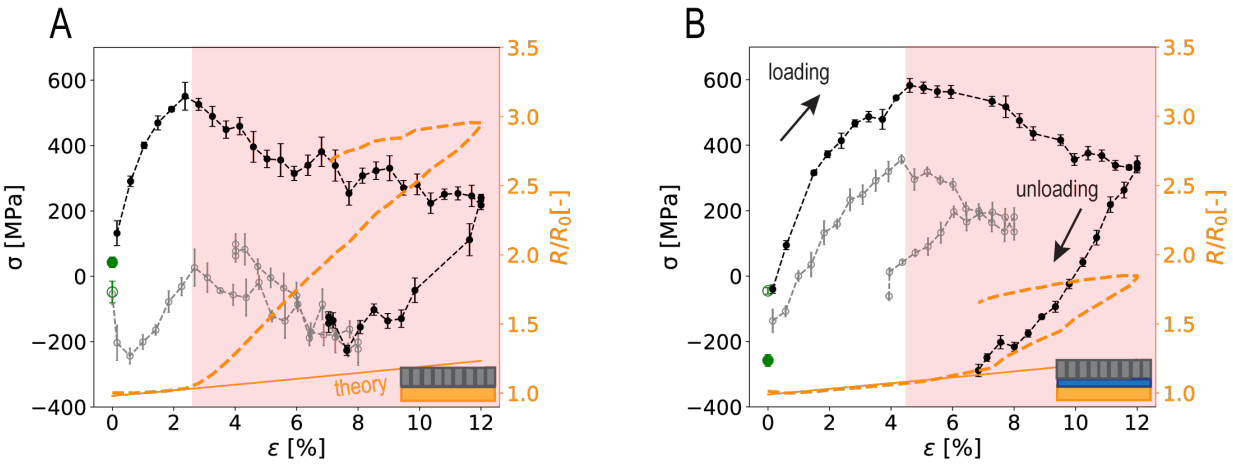

Figure 3: Al film stress and normalized resistance as a function of applied strain (loading and unloading), measured from in–situ XRD uniaxial straining experiments. A: Al/PI native interlayer system with a failure strain of 2.5% and B: Al/am–AlO_xH_y/PI artificial interlayer system with a failure strain of 4%. Axial and transverse stresses are shown with filled black and open grey symbols, respectively. Corresponding residual stresses are marked with a filled (axial) or open (transverse) green circle. X error lies within the plotted datapoints and is thus not visible. Note that in the transverse direction, films were only strained to 8%. The area from the maximum stress to the end of loading is marked with a red overlay, indicating the strain range where thin film failure is taking place. Electrical resistance measured during the axial stress measurement are marked with orange dashed lines. Theoretical resistance increase is marked with solid orange lines.

resistance. Before cracking at 2.5%, the stress strain curve is not linear, indicating possible plastic deformation. Upon further loading, the stress relaxes linearly until approximately 6% strain, at which point the stress relaxation rate decreases until the maximum applied strain of 12% is reached. This rate change can be attributed to an overlap of stress relaxation zones at the crack edges.[39] During unloading, there is an initial stress drop due to load reversal, followed by a plateau–like compressive state around –180 MPa. Compressive stresses are induced in the film upon unloading as a result of continued elastic relaxation of the polymer substrate.[29] In contrast, the artificial interface system exhibits more ductile behavior, gradually reaching the ultimate tensile strength $\sigma_{x_{max},art.} = 588 \pm 20$ MPa) around 4.5% applied strain (= failure strain). Increased non-linearity of the stress-strain curve before mechanical failure indicates more plasticity compared to the artificial interlayer film. This is followed by a stress plateau and stress relaxation around 7% strain, coinciding with the deviation of the electrical resistance from the theoretical prediction, at much higher strains than for the native interlayer system. During unloading, compressive stress accumulates linearly.

In the transverse direction, the initial stress evolution before fracture (grey curves in Figure 3 A and B) can be explained via a combination of Poisson's ratio mismatch and two–dimensional shear lag.[38] As the Al thin film starts to deform, its (apparent) Poisson's ratio changes from 0.33 (linear elastic deformation regime) to 0.5 (plastic deformation regime).[40] Meanwhile, the polyimide substrate still deforms with a Poisson's ratio of 0.32, leading to a lateral constriction and the development of tensile stresses in the metal thin film on the polyimide substrate.[16] Once cracks start to form, transverse stresses start to drop in both films (peak in grey curves, Figure 3 A and B), either through a relaxation mechanism or the build up of compressive stresses. This can be explained by the substrate deforming elasto–plastically in this strain region, constraining the Al thin film, which is no longer undergoing plastic deformation.[9] Transverse compressive stresses after crack onset are corroborated by Frank *et al.*, however, the more ductile nature of Al films prevents direct comparison with their model derived for brittle thin films.[38] Note that films were only

strained up to 8% in the transverse direction. During unloading, the two systems show very different transverse stress behavior, due to more plasticity with the artificial ALD interlayer. Specifically, the native and artificial interlayer systems return to a stress–free state, either from compressive or tensile stress levels. This transverse stress–strain behavior is comparable to Al (multi)layer films tested uniaxially in Putz *et al.*, where the transverse unloading sections show the same behavior: compressive and tensile stress regimes for more brittle and ductile systems, respectively.[28]

For both interface systems, $\sigma_{x_{max}}$ and $\sigma_{y_{max}}$ align well, indicating good correlation of the axial and transverse datasets and substantiating the definition of thin film failure, highlighted in red in Figure 3. Additionally, the transverse stress behavior attests good adhesion to both film systems in this strain regime, as transverse compressive stresses are not relaxed during loading.[38] We can conclude from this uniaxial test campaign that the addition of our artificial ALD interlayer between the polyimide substrate and the Al thin film increases fracture strain and improves fracture behavior, i.e. increases ductility of the Al layer.

The influence of thin film microstructure on stress–strain behavior is evident from equi–biaxial in–situ diffraction tensile testing, constituting also a highly application–relevant loading scenario. Figure 4 A and B show the evolution of Al film stress, full width half maximum (FWHM at $\chi = 90°$ (= ψ 0°), Al (111) peak) and electrical resistance during loading and unloading for native and artificial interlayer systems with larger and smaller grain size, respectively. FWHM peak broadening can be correlated to increasing defect density and strain heterogenities in the thin film.[41] The FWHM data and resistance also aid in determining different deformation regimes and behaviour.[42] Curves for FWHM data at all χ angles are provided in the supporting information (Figure S3), with trends corresponding to FWHM data at $\chi = 90°$.

Residual stresses (green crosses in Figure 4, $\sigma_{res.,nat.,bi} = -13 \pm 2$ MPa, $\sigma_{res.,art.,bi} = -120 \pm 5$ MPa) indicate a neutral / slightly compressive initial stress state before loading, following the same trend as the uniaxial samples with respect to the interface structure. The larger

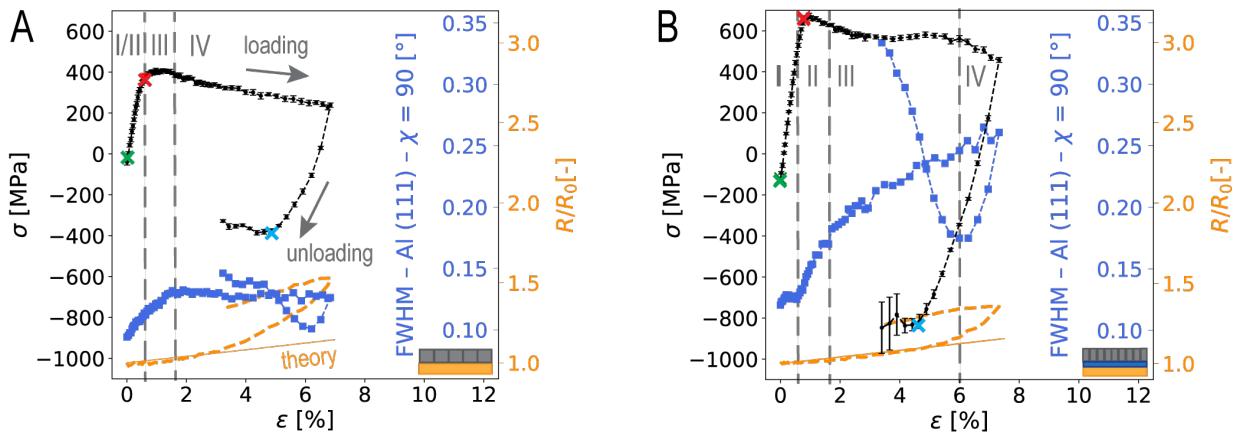

Figure 4: Al film stress (black), FWHM (Al (111) peak, blue) and normalized resistance (orange) as a function of applied strain (loading and unloading), measured from in–situ XRD equi–biaxial straining experiments. X error lies within the plotted datapoints. A: Al/PI native interlayer system. B: Al/am–AlO_xH_y/PI artificial interlayer system. Vertical grey dashed lines illustrate different deformation domains during loading (I: elastic, II: micro–plastic, III: necking, IV: fragmentation). Measured electrical resistance and theoretical prediction are marked with orange lines. Measured residual and calculated 0.2% yield stresses are marked with green and red crosses, respectively. The compressive yield stress during unloading is indicated with a blue cross. Note the grain size difference between A and B.

grain size of the native interlayer system (Figure 2, also reflected in smaller initial FWHM values), likely contributes to increased plasticity and a more ductile deformation behavior compared to uniaxial tension (Figure 3 A), as larger grains act as sites of strain localization and subsequent film thinning, eventually leading to local delamination and failure.[43] Based on stress and FWHM data, the loading portion can be classified into four deformation domains: elastic (I, stress–strain increase linear, FWHM typically constant), micro–plastic (II, stress–strain curve bends over, FWHM increases as dislocations start to nucleate), necking/localized plastic deformation (III, stress constant, FWHM increasing with a different slope) and fragmentation (IV, stress decreasing, FWHM constant, deviation of resistance from theoretical prediction).[44] As a result of strain heterogenities induced by large grains or higher roughness, this film does not show a clear FWHM plateau in domain I, therefore regime I and II cannot be clearly distinguished.[28]

The artificial interlayer film exhibits similar deformation domains I–III, whereby the 0.2% yield stress of 667 ± 5 MPa is significantly higher than its native counterpart ($\sigma_{yield,nat.}$ = 382 ± 10 MPa). In Domain II and III (micro–plasticity and necking) the increase in FWHM is more pronounced, possibly indicating increased plasticity and dislocation activity.[28] Compared to the native interlayer film, this system exhibits fracture at higher strains (6% vs. 1.5%), as stresses are relaxed by through–thickness cracking and crack opening, with FWHM staying constant (domain IV) and resistivity deviating from theoretical values later. Post–mortem SEM imaging (see supporting information Figure S4) evidenced damage in both samples, indicative of equi–biaxial straining.[42] Quantification, however, is difficult due to crack closure upon unloading. Deformation densities were measured as 1.47 and 1.34 μm/μm^2 for native and artificial interlayer systems, respectively. Differences in deformation patterns are discussed in detail in section 2.3, where samples were strained to higher strains and crack patterns are much more developed.

Assuming that the smaller dimension of grain width, as opposed to the film thickness, controls the yield stress, the observed difference between samples can be explained by grain

size d according to the Hall–Petch relation ($\sigma_{yield} = \sigma_0 + K * d^{-\frac{1}{2}}$, with $\sigma_0 = 11.3$ MPa the bulk strength and $K = 0.07$ MPa $\mathrm{m}^{\frac{1}{2}}$ the Hall–Petch constant).[45–47] From grain sizes measured via ACOM, the expected yield stresses were calculated from the Hall–Petch equation as $\sigma_{yield,nat.,H-P} = 178$ MPa and $\sigma_{yield,art.,H-P} = 404$ MPa. For the native interlayer with a bigger grain size which approaches the TEM lamella thickness, a correction factor of $\frac{\pi}{2}$ was applied to account for FIB slicing effects.[48] Calculated yield stresses underestimate experimentally measured ones. As H–P does not take into account differences in film thickness, the Nix approach was used to include potential strengthening effects of a reduced Al film thickness in yield stress calculations.[49] Both equations and used parameters are provided in the supporting information in section S5. The calculated yield stresses with both grain size and film thickness contribution are $\sigma_{yield,nat.,Nix+H-P} = 378$ MPa and $\sigma_{yield,art.,Nix+H-P} = 587$ MPa, with the artificial interlayer system being stronger experimentally than theoretically calculated, which could stem from additional interface strengthening. Interlayers (native or artificial) are excluded from the calculations.

There is evidence in the unloading data that the two interface types act differently with respect to dislocation storage. One obvious difference in the unloading behavior between the two systems is the amount of FWHM recovery. For the native interlayer film, the FWHM curve recovers almost fully to original values (94% recovery), associated with partial dislocation nucleation and absorption at grain boundaries for grain sizes or film thicknesses $<$ 100 nm.[28] Dislocations also impinge upon and disappear in the native Al/PI interface, which can offer additional FWHM recovery for the native interlayer film.[18] Conversely, the artificial interlayer film does not exhibit the full recovery of FWHM expected based on grain size (only 70% recovery), pointing towards the artificial interface promoting dislocation storage in the metal film. The same trend is observed in uniaxial FWHM data (supporting information Figure S2). FWHM evolution after recovery mirrors the loading portion of the experiment, with a slight increase and plateau vs. steep increase for the native and artificial interlayer film, respectively. Using the end of the stress–strain curve's linear region and the FWHM

increase after unloading as reference points, the compressive yield stress was determined as $\sigma_{compr.,nat.}$ = –377 ± 11 MPa and $\sigma_{compr.,art.}$ = –816 ± 35 MPa for native and artificial interlayer system, respectively, close to the tensile values.

Besides mechanical strength, it is important for flexible applications that thin films are equipped to maintain functional properties under load. For both uni–and equi–biaxial straining experiments, electrical resistance was recorded in–situ and normalized by the initial resistance R_0 (Figure 5 A–B). During loading, due to changes in geometry, the resistance ratio R/R_0 increases according to $R/R_0 = L/L_0 = (1+\varepsilon)^2$ (with gauge length L and initial length L_0, green dashed line in Figure 5, orange lines in Figures 3 and 4).[50] This constant volume approximation holds for both electrical resistance setups used in this work. Cracking of the film causes the resistance to deviate from the theoretical trend (crack onset strain, COS) and electrical failure is defined in the literature as a 10% deviation (red dashed line in Figure 5).[28] The corresponding strain value will be denoted as electronic failure strain (EFS) and is indicated with vertical solid lines in Figure 5.

The different microstructure of our Al layers (see Figure 2) results in initial resistivity values of 5 and $7 * 10^{-8}\,\Omega$m for larger and smaller grains, respectively, with no measurable contribution from the ALD interlayer. Our measurements are comparable to literature values of magnetron–sputtered thin films.[29]

Figure 5 A and B summarize the normalized electrical resistance data for uni–and equi–biaxially strained samples, corresponding to the diffraction data shown previously. Both Al films with native interlayers (smaller and larger grain size, Figure 5 A), fail at low EFS values around 4% (EFS 3.5% / COS 2.7%, uniaxial and EFS 4.5% / COS 2.5%, biaxial), whereby observed differences between loading conditions are likely dominated by the microstructure. The Al films with artificial interlayers (Figure 5 B), on the other hand, can sustain up to three times higher applied strain before electronic failure. Based on identical Al microstructures, we can note that multiaxial loading (EFS 6.8% / COS 5%) accelerates electrical failure (uniaxial: EFS 8.5% / COS 6.5%), even if performed at a lower strain rate.

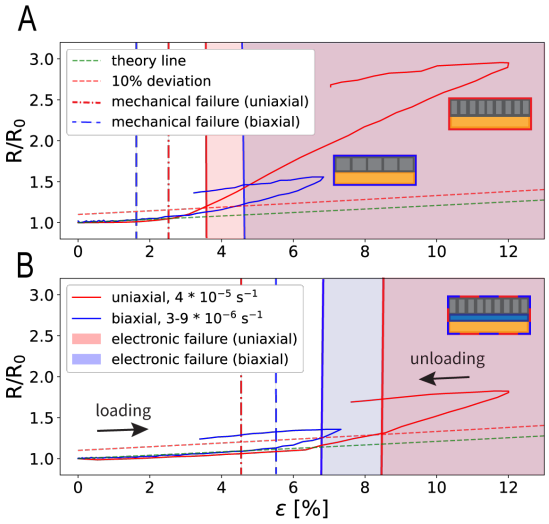

Figure 5: Normalized electrical resistance data of Al films as a function of applied strain. A: Al films with native interlayer (Al/PI) and B: Al films with artificial interlayer (Al/am–AlO_xH_y/PI). Theoretical resistance increase and 10% deviation thereof are marked with green and red dashed lines, respectively. The strain range where samples reach the electrical failure limit is marked in light red (uniaxial straining) and light blue (biaxial straining). Mechanical failure measured from XRD measurements is indicated with red dashed-dotted (uniaxial) and blue dashed (biaxial) lines. Errors are within 0.003 of R/R_0 (measurement accuracy according to datasheet).

Damage in an equi–biaxially strained thin film evolves in a mudcrack pattern as opposed to unidirectional fragmentation.[42] Overall, these resistance results correlate well with the stress–strain data (XRD failure strains indicated with vertical dashed lines), where stress relaxation through cracking is initiated at later strains for all artificial interlayer film systems. The compressive Al residual stress state induced by the ALD interlayer is expected to contribute to this improvement. Concurrently, also a lower total resistance increase (R/R_0 at equivalent ε_{max}) is observed compared to their native interlayer counterparts. Upon unloading, normalized resistance decreases in all cases as crack flanks close, however, complete recovery is not possible due to oxidation effects and to plastic deformation of the Al surrounding the crack, which prevents realignment of crack faces. We can conclude that the addition of an artificial amorphous interlayer is effective in delaying the onset of the fragmentation process and in conserving electric conductivity at higher strains.

2.3 Crack patterns and adhesion

To assess the influence of the artificial ALD interlayer on crack patterns and adhesion, AFM surface measurements were performed on small-grained Al films (see Figure 2 B and C) previously strained to 40%, of which representative results are shown in Figure 6. At such high strains, crack closure due to relaxation of the polymer is minimized, allowing imaging of the developed crack pattern after unloading. The corresponding in–situ electrical resistance data are provided in the supplementary material in Section 5 (Figure S5).

The Al film with native interlayer (Figure 6 A) exhibits straight through–thickness cracks perpendicular to the tensile direction, indicated by black arrows. Brittle cracking is confirmed by the corresponding AFM surface profile (Figure 6 B) that shows steep crack flanks. Large triangular buckles, marked with white circles, form at the crack flanks due to compressive stresses in the transverse direction.[38] FIB/SEM cross–sections (Figure 6 A, top) confirm this phenomenon by showing local delamination of the Al film from the polymer substrate. The development of transverse compressive stresses after crack onset is evident in Figure 3 A. Adhesion energy was calculated from buckle geometry using the tensile induced delamination (TID) method as 13.4 ± 3.1 J/m^2.[32] The corresponding adhesion plot and analysis are provided in the supporting information (Figure S5 A). The value is comparable to literature values of Al on polyimide and a range of magnitude higher than for brittle thin films such as WTi or Ti on polyimide.[51]

The Al film with artificial ALD interlayer (Figure 6 B) shows shorter cracks following a zigzag pattern. Smaller and fewer buckles (confirmed by FIB cross–section in Figure 6 B) form compared to the native interlayer system, attesting to better adhesion. This is quantitatively supported by a calculated adhesion energy value of 23.9 ± 5.0 J/m^2, with the corresponding adhesion plot and analysis provided in the supporting information (Figure S5 B). The AFM image shows an increased amount of localized plastic deformation, that is, necking occurs before through–thickness cracks form, resulting in tapered crack flanks in the extracted surface profile in Figure 6 D. Increased plasticity in this film is supported

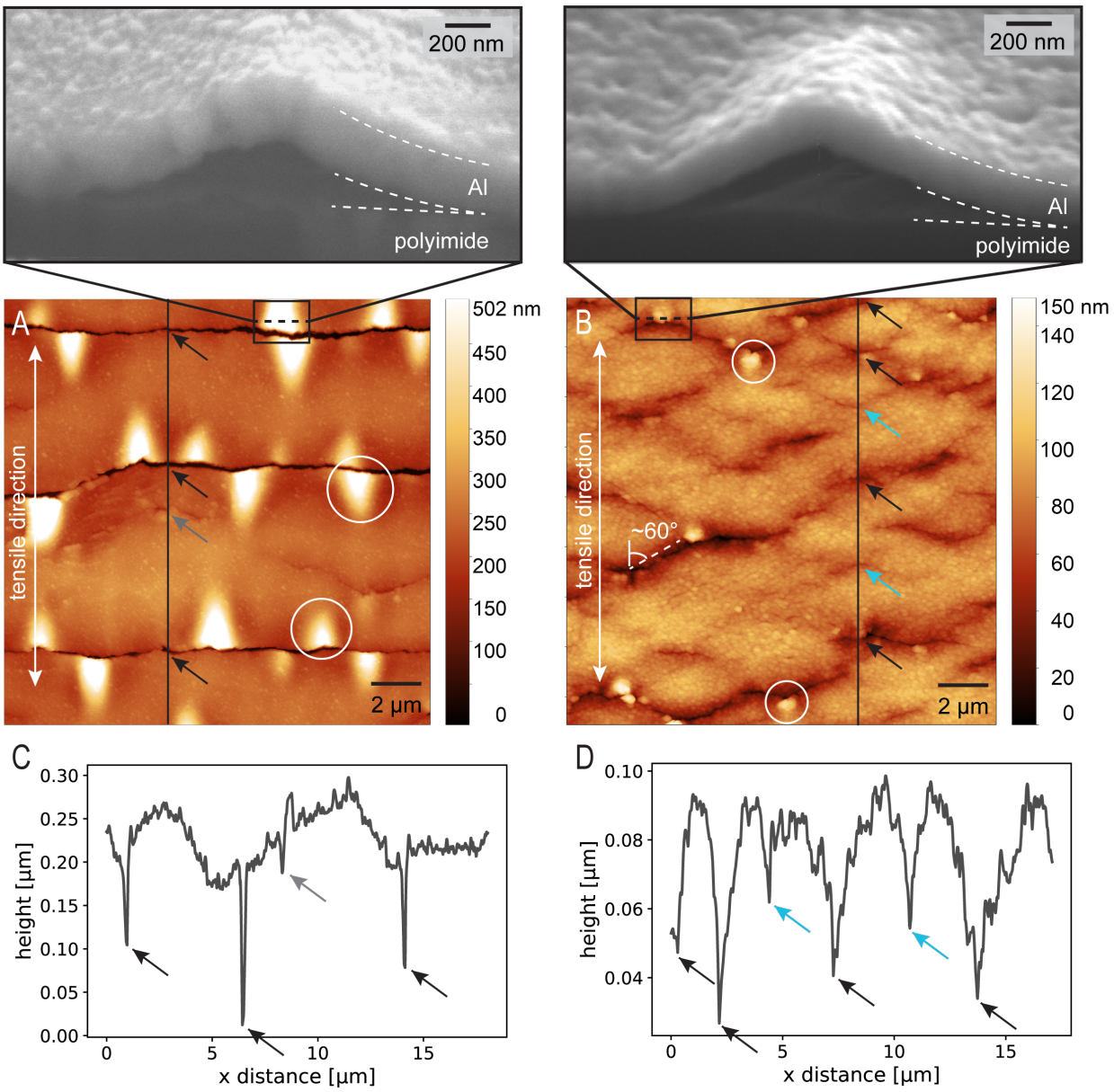

Figure 6: Post–mortem analyis of thin film cracking and local tensile induced delamination. Native (A, B) and artificial (C, D) interlayer systems strained to 40%. AFM images of the film surface (A, B) show the presence of buckles (white circles), cracks (black arrows), and necking (blue arrows). Corresponding FIB/SEM cross–sections at the top show areas where the Al film locally delaminated from the polyimide substrate, forming a buckle. A grey arrow in A and B marks a developing brittle crack. The tensile direction is marked with a white double–headed arrow. Black vertical lines in A and B mark the position of corresponding surface profiles C and D. Note the different height scales for AFM images and surface profiles.

by the pronounced non-linear behavior of the stress-strain curve before mechanical failure (Fig. 3 B). Lassnig *et al.* established how a higher amount of plastic deformation during buckling corresponds to higher adhesion energy values.[14] Lu *et al.*[15] demonstrated that by improving surface bonding and therefore constraining the metal thin film, strain localization and debonding are suppressed, preventing cracking.

Necking and through–thickness cracking was quantified via applying a Δ/h ratio $> 15\%$ criterion (Δ being the penetration depth of the AFM tip and h being the film thickness) to the surface profiles in Figures 6 C and D. Using this criterion, saturation through–thickness crack (TTC) spacings for both systems were measured as $\lambda_{TTC,nat.} = 4.41 \pm 1.42$ μm and $\lambda_{TTC,art.} = 4.00 \pm 2.22$ μm for native and artificial interlayer systems, respectively. Features with a Δ/h ratio $< 15\%$ where classified as deformation (gray/blue arrows Fig. 6 C,D) and excluded from the analysis. Necks only substantially featured in the artificial interlayer system, for which the total deformation spacing $\lambda_{def,art.}$ was measured as 3.52 ± 1.32 μm. Using saturation crack or deformation spacings $\lambda_{sat.}$, the maximum tensile strength σ_{max} and the film thickness h, the interfacial shear strength τ_{IFSS} can be calculated:[52]

$$\tau_{IFSS} = \frac{3\pi}{4}\frac{h}{\lambda}\sigma_{max} \tag{1}$$

This approach yields $\tau_{IFSS,TTC,nat.} = 96 \pm 32$ MPa and $\tau_{IFSS,TTC,art.} = 111 \pm 62$ MPa. Including necks and using the saturation deformation spacing, interfacial shear strength was calculated as $\tau_{IFSS,def.,art.} = 126 \pm 47$ MPa for the artificial interlayer system. In both cases, the artificial interlayer system has a larger interfacial shear strength, however, large standard deviations of $\lambda_{sat.}$ preclude a clearer distinction between the two sample systems.

The noticeable difference in the angles at which the cracks develop aligns with adhesion energy and interfacial shear strength results. For the native interlayer system, cracks form at almost 90° relative to the tensile direction, while they form at varying angles between 60° and 90° for the artificial interlayer system with doubled adhesion energy. These zigzag crack patterns are comparable to ductile copper films on polyimide, and have been analytically

justified using bifurcation analysis, where it was demonstrated that the ability of a metal film to deform plastically is influenced by how well the film adheres to the underlying substrate, with better adhesion leading to increased ductility.[15,16] Furthermore, effective crack lengths, experimentally difficult to measure, can be calculated from the saturation crack spacing and in–situ electrical resistance data (R/R_0 at 40% strain).[53] Lower and upper limits for effective crack lengths were calculated as $l_{0,nat.}$ = 28.2–54.9 μm and $l_{0,art.}$ = 1.7–5.8 μm, taking into account the distribution of crack spacings. These values correspond well to Figure 6 C and D and can explain the different electrical resistance behavior (red curves in Figure 5 A vs. B): shorter cracks in the artificial interlayer system leave more percolation paths for electrons, conserving electrical conductivity at higher strains. Finite R/R_0 values at 40% strain, even for the native interlayer system (see Figure S6 in supporting information), are due to brittle cracks being shorter than the sample width (5 mm).

The poor electromechanical and adhesive behavior of our sputter–deposited Al with native interface is in contrast to most established and recent literature, attributing high interface quality to the naturally forming Al–O–C complex.[18,28,33] Only without previous surface activation of the substrate, the formation of a sharp oxide layer instead of a diffuse Al–O–C interface has been associated with lower adhesion.[24] As such, the oxide character of the thin layer identified in TEM–EDX (grey area in 1 C ii), could contribute to adverse brittle failure and through–thickness channel cracking. Chemical reactions responsible for native interlayer formation might be compromised by our room–temperature deposition. The smaller grain size of our Al films compared to literature (around 100 nm at comparable film thicknesses) would also contribute to more brittle behavior, however, this is apparently fully compensated by the ALD interlayer.[28,29] With identical microstructure, improved electro–mechanical properties can be clearly attributed to the artificial interface structure. Enhanced interfacial adhesion suppresses brittle cracking and facilitates plasticity with shorter and more angled cracks delaying electrical failure.[15]

Although the above-mentioned activation of polymer surfaces through plasma treatment

does result in adhesion promotion for selected material systems, it also involves the risks of transmitted surface roughness at low film thicknesses and unintended fragmentation of polymer chains in the surface layer.[24,54] This damage leads to unpredictable, time-dependent adhesion phenomena, including complete adhesion loss and delamination. As susceptibility to chain fragmentation strongly depends on polymer chemistry and aggressiveness of the plasma, this approach has limited applicability, and materials restrictions remain. Similarly, promoting adhesion and selective crack suppression through electron beam irradiation is limited to small surface areas and prone to induce topography.[55,56] A recent approach has been made using self-assembled monomolecular layers at the interface, however, this also requires aggressive O_2 plasma treatment of the polymer surface.[57] In contrast, ALD is a mild process, suitable for a wide range of sensitive polymers prone to plasma damage, and scalable as the self–limiting aspect (layer–by–layer growth) can be maintained beyond vacuum–pumped reaction chambers using spatial atmospheric ALD, compatible with roll–to–roll processing of polymer sheets, typically using metal evaporation rather than sputtering.[58] It could, as such, easily be transferred to other metal or oxide thin films on polymers with polar functionalities. Other material systems that would greatly benefit from ALD interface engineering include Al–Polypropylene, where the lack of polar functional groups and a difference in surface energy inhibits adhesion or systems without intermixing, such as Al/FEP.[23] However, polymers without polar functionality may not allow easily to chemically bind the ALD precursor and instead a physical trapping can occur upon Vapor Phase Infiltration (VPI, detailed in following paragraphs). In certain cases, sub-surface growth of physically trapped particles has been reported, whereby the degree of their mobility could impact the potential for stabilizing the Al thin film, necessitating further experimental validation.[59–61]It has been experimentally demonstrated for polymers without polar functionalities (PE, PP, PTFE and PDMS) that clusters of ALD material formed in the near-surface region of the polymer coalesce after a certain number of ALD cycles (25-30), ultimately forming a continuous thin film.[60]As such, it would be expected that from a certain cycle number, the PVD Al coating

would be stabilized.

Other commonly used interlayers (Cr, Mo, W, Ti, ...) promoting adhesion of ductile metal films are prone to dominate and deteriorate electro–mechanical properties through stress concentration at local fracture sites.[16] In contrast, we have no evidence of embrittlement induced by the amorphous AlO_xH_y interlayer for either the uni–or biaxial straining states using our ALD approach. Following the expected behavior for metals, the Al film with ALD interlayer is stronger in equi–biaxial tension compared to uniaxial tensile loading.[42] Compared to the native interlayer, where dislocations can impinge upon and disappear in the interface, a different interface–driven process is activated, such that dislocations, blocked by the ALD layer, are stored in the nanocrystalline Al films.[18] While deformation of the interlayer itself cannot be traced directly with the presented XRD and post–mortem SEM/FIB approach, we expect ductile behavior for ALD–Al_2O_3 up to a thickness of 5 nm, based on recent literature studying confinement between metallic layers.[28,29,62] As layer order influences failure mechanisms in flexible systems, proximity to the polymer substrate as interlayer is expected to further enhance ductility.[44]

The heightened hydrogen content in our AlO_xH_y interlayer, on the other hand, could reduce room-temperature plasticity, with hydroxyl bonds acting as weak links for a crack to propagate easily.[37] This negative influence of hydrogen rich regions promoting brittle fracture is seen on amorphous silicon oxide films.[63] H contamination can be controlled via the ALD deposition temperature.[37] Using the combined ALD/PVD chamber without active substrate cooling requires a minimum 2.5 h waiting period cooling from ALD deposition temperature (120 °C for Al_2O_3) to RT between depositions. Alternatively, for temperature-sensitive substrates, plasma-enhanced ALD is known to result in low H content, even for deposition at RT.[64] However, as with surface activating plasma treatments, this method could damage the surface layer of the polymer substrate.[54]

At low ALD processing temperatures, the nucleation behavior must also be considered, with amplified vapor phase infiltration (VPI) of polymer substrates.[35] Evidence of this sub-

surface hybrid layer growth mechanism might be seen in HR-TEM as a narrow bright region directly underneath the ALD layer (transition region 1 B). This hybrid layer may enhance durability by absorbing the energy released upon crack formation, as observed in bending tests of ALD-Al_2O_3 on polyamide (PA6).[35] Compared to extensive hybrid layer growth on PA6 (depth of 120 nm at 60 °C for 100 ALD cycles), our potential VPI zone is limited to a few nm only. For Kevlar fibers, infiltration with only a few nanometers of ALD-Al_2O_3 already improves the mechanical properties of the polymer.[59] As such, it is possible that shallow VPI is an additional mechanism contributing to the mechanical stabilization of the thin films in our study.

3 Conclusion

Uni– and equi–biaxial tensile straining with in–situ XRD and electrical resistance measurements was carried out on sputter–deposited Al–polyimide films with and without an adhesion–promoting amorphous AlO_xH_y artificial interlayer. Nanocrystalline Al reference films without ALD exhibit brittle cracking, associated with early electrical failure and low adhesion energy. Adding an artificial ALD interlayer significantly improves the thin film system across multiple performance metrics:

- *Mechanical properties:*Enhances ductility and increases failure strain by inducing compressive residual stress and enabling dislocation activity and localized plastic deformation, as evidenced by FWHM measurements that indicate effective dislocation blocking at the interface and storage within the metal layer.

- *Interfacial strength:* Doubles the adhesion energy (23.9 ± 5.0 compared to 13.4 ± 3.1 J/m^2) and increases interfacial shear strength, resulting in shorter, non-continuous cracks upon straining.

- *Electronic performance:* Provides a substantial increase in crack onset and electronic failure strains, maintaining conductivity at higher strain levels.

There is no evidence of embrittlement associated with other common adhesion interlayers under either loading condition. Currently, it is unknown to what extent and by which mechanism the H content in our ALD interlayer influences adhesion. Future research should also focus on investigating the fatigue behavior of our interlayer systems, as well as variation of ALD interlayer thickness. Considering the sub–nanometer thickness control of ALD, there might be room for further optimization of interface quality and electro–mechanical properties within the thickness range of 0.14–5 nm, also in view of optimized material consumption. Our mild and scalable interface engineering method constitutes a major first step forward in controlling interface quality and tailoring electromechanical properties and is transferrable to other metal–polymer combinations. The significant enhancement in strain tolerance achieved in this work enables device conformability to complex curved surfaces while preserving functional performance and marks a crucial milestone for the design and development of deformation–resistant materials for flexible electronics and space applications.

4 Experimental

4.1 Synthesis of thin film systems

Al thin films (170 nm nominal thickness, PVD) were sputter–deposited on a polyimide (PI–DuPont Kapton® HN) substrate, both with and without an amorphous (am)–AlO_xH_y interlayer. ALD of the interlayer was performed at room temperature (RT) using a precursor sequence with the following pulse–exposure–purge: $Al(CH_3)_3$ (TMA, Dockweiler Chemicals GmbH), 0.2–0.5–20 s and H_2O, 0.15–1–20 s for 36 cycles, nominal thickness 5 nm. The deposition resulted in an am–AlO_xH_y layer with a growth per cycle (GPC) of 0.14 nm, which is comparable to values reported in literature for RT alumina ALD.[34] The polymer substrates were pre–cut into testing geometries (tensile strips of 5 x 0.6 cm and cruciforms with an arm width of 20 mm, see[65]) to avoid post–deposition etching and edge effects.

All substrates were ultrasonically cleaned in acetone and isopropanol (5 min each) prior to deposition. The depositions were done using a combined ALD–PVD setup (Figure 7, SC–1 from Swiss Cluster[66]), using two equidistant planar Al targets (diameter 50.8 mm, purity 99.999%, HMW Hauner GmbH, substrate to target distance 110 mm) without substrate rotation. Sputtering conditions for Al layers (summarized in Table S1 in the Supporting Information) include a current of 280 mA, a base pressure lower than 2×10^{-5} mbar, a working pressure of 7–9 $\times$ 10^{-3} mbar and a combined deposition rate of 0.075–0.081 nm/s. For cruciform substrates, a mask was used to deposit thin film squares with 1 cm side length in the center of each crucible.

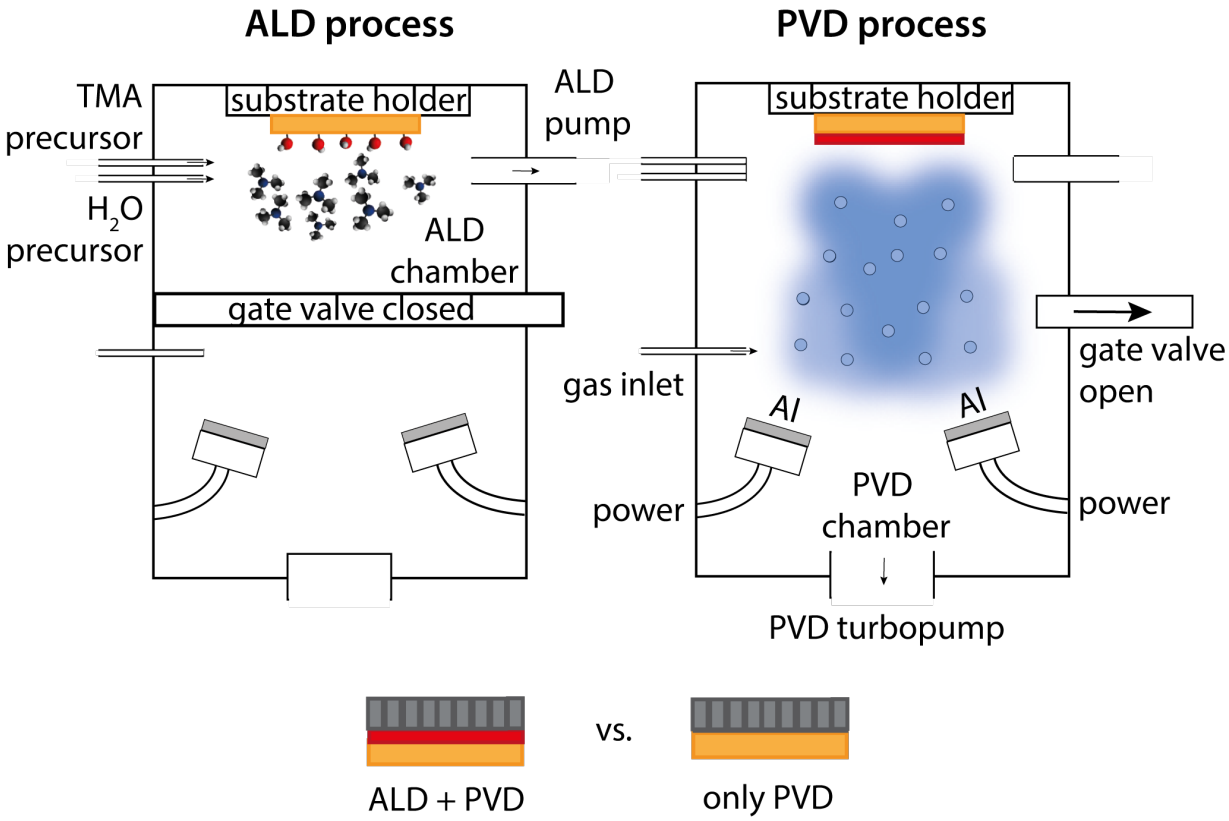

Figure 7: Schematic illustration of the combined ALD-PVD process used for metal-polymer interface engineering. The left-hand side of the graphic shows the ALD process, while the right-hand side shows the PVD process. The substrate holder is positioned at the top of the chamber inside the ALD chamber, which is connected to the PVD chamber by a gate valve that can be opened or closed dependent on the process. Adapted from drawing provided by the manufacturer (Swiss Cluster).

4.2 Microstructural and chemical characterization

TEM (FEI Titan Themis 200, ThermoFisher, 200 kV) analysis ascertained Al grain size and layer thickness of both the Al layer and the artificial interlayer, following FIB (Tescan Lyra/XMU Dual beam FIB: 240 pA for rough cutting, 45 –10 pA for polishing) cross–sectioning and liftout (lamella thickness 100 nm). As the room temperature ALD process took place outside of the established ALD window for alumina (100–120 °C[37]), a thick AlO_xH_y ALD sample (525 cycles, nominal thickness 75 nm, precursor sequence see above), was characterized chemically using rutherford backscattering (RBS) and elastic recoil detection analysis (ERDA) on Si wafer and Kapton polyimide substrates.

4.3 Electromechanical testing

The deposited (bi–)layer films on polyimide were subjected to uni–[29] and equi–biaxial[67] tensile loading and unloading with in–situ X–ray diffraction (XRD) and electrical resistivity measurements at synchrotron radiation facilities BESSY II (KMC–2 beamline[68]) and SOLEIL (DIFFABS beamline[69]), respectively. XRD (Al (111) Bragg reflection; KMC–2: wavelength 0.128 nm, spot size 250 µm, Bruker VÅNTEC 2000 detector, $\sin^2\psi$ analysis: 5 ψ angles 0° –45°; DIFFABS: wavelength 0.128 nm, spot size 300 µm, XPAD–S140 detector, $\sin^2\psi$ analysis: 8 ψ angles 0°–70°) was performed to measure lattice strain. For uniaxial straining, both longitudinal and transversal Al lattice strains were measured, parallel and perpendicular to the tensile direction, respectively. Data was evaluated using a custom Python 3 routine with pseudo–Voigt and Pearson VII function fitting. Lattice stress was calculated using X–ray elastic constants (XECs, 1.8436 10^{-5} Pa for untextured Al (111) reflections, calculated from single–crystal elastic constants using the Hill model and the software ElastiX.[70] No XRD signal was obtained from the artificial interlayer due to its amorphous nature and low thickness.

Uniaxial tests were carried out using an Anton Paar TS600 device (maximum strain ϵ_{max} = 12%, strain rate 4 $\times 10^{-5}$ /s), with resistance probes incorporated into the grips. The

equi–biaxial experiment (preload 3 N, maximum strain $\epsilon_{max} = 8\%$, strain rate 3 –9 $\times 10^{-6}$ /s) included an in–situ 4–point–probe Van der Pauw resistivity setup.[31] Macroscopic strains (ϵ) were correlated to lattice strain via Digital Image Correlation (DIC, on the backside of the samples).[42]

After straining, post–mortem SEM (Hitachi S–4800, Japan, 1 kV) images were analysed to obtain crack density and spacing for both equi–and uniaxial samples.

4.4 Adhesion measurements

To induce buckling, samples of each interface structure were uniaxially strained to 40% using a MTS Tytron 250 tensile testing machine with a quasi 4–point probe electrical resistance setup (Keithley 2000 multimeter) integrated into the grips. Five post–mortem AFM (Cypher AFM, Asylum Research) images were used to determine saturation crack spacing and buckle geometry. Through–thickness cracks, as opposed to necking, were classified as having a Δ/h ratio $> 15\%$ (Δ being the penetration depth of the AFM tip and h being the film thickness) from extracted surface profiles.[16] Adhesion energy was calculated from the buckle geometry using the TID method, measuring 40 buckles per condition.[32] Delamination at the metal–polymer interface was ascertained using FIB cross–sectioning (Tescan Lyra/XMU Dual beam FIB: 240 pA for rough cutting, 45–10 pA for polishing) and SEM imaging.

Acknowledgement

The authors thank A. Müller from the Laboratory of Ion Beam Physics at ETH Zürich for RBS/ERDA measurements, D. Gutnik for discussions on adhesion analysis, and R. Spolenak for general discussion. We thank HZB for the allocation of synchrotron radiation beamtime (231–11757–ST). SOLEIL is gratefully acknowledged for the beam time allocation (Proposal 20220220, DIFFABS beamline). The authors thank the KMC–II (Daniel Toebbens) and DiffAbs beamline teams (Cristian Mocuta) for technical help during the experiments described

in this paper. P.O.R. acknowledges funding from ANR-18-EURE-0010. J. B. and B. P. acknowledge funding from the Swiss National Science Foundation under the Ambizione grant agreement No. PZ00P2_202089. C.O.W.T. gratefully acknowledges the financial support under the scope of the UFO program (SPM –PN 3022) by the Austrian State of Styria (Land Steiermark –Abteilung 12 Wirtschaft, Tourismus, Wissenschaft und Forschung). T.E.J.E. acknowledges funding from the European Union's Horizon 2020 research and innovation programme under the Marie Skłodowska-Curie grant agreement No. 840222.

CRediT authorship contribution statement

J. Byloff: Conceptualization, Investigation, Visualization, Writing–Original Draft Preparation, Writing - Review & Editing

C. Trost: Investigation, Methodology, Software, Validation, Writing–Review & Editing

V. Devulapalli: Investigation, Writing–Review & Editing

D. Faurie: Investigation, Methodology, Validation, Writing–Review & Editing

P.–O. Renault: Investigation, Methodology, Software, Writing–Review & Editing

T. E. J. Edwards: Investigation, Writing–Review & Editing

M. J. Cordill: Investigation, Funding Acquisition, Methodology, Writing–Review & Editing

D. Casari: Investigation, Writing–Review & Editing

B. Putz: Conceptualization, Funding Acquisition, Project Administration, Supervision, Writing–Review & Editing

Supporting Information Available

Supporting Information includes: PVD deposition parameters, additional IPF-y maps, FWHM evolution at different χ angles, post–mortem SEM images of biaxially tested samples, the theoretical yield stress and adhesion energy calculations, and additional resistance curves.

References

(1) Liaw, D.-J.; Wang, K.-L.; Huang, Y.-C.; Lee, K.-R.; Lai, J.; Ha, C. Advanced polyimide materials: Syntheses, physical properties and applications. *Progress in Polymer Science* **2012**, *37*, 907–974.

(2) Moery, J. Development of robust thermo-optical thin-film membranes for the James Webb Space Telescope sunshield. *Space Telescopes and Instrumentation I: Optical, Infrared, and Millimeter* **2006**, *6265*, 62653B.

(3) Montinaro, N.; Cicero, U. L.; D'Anca, F.; Bozzo, E.; Paltani, S.; Barbera, M. Elastic characterization of nanometer-thick polymeric film for astrophysics application with an experimental-numerical method. *Journal of Astronomical Telescopes, Instruments, and Systems* **2023**, *9*, 34005 – 34035.

(4) Haight, R. Electron dynamics at surfaces. *Surface Science Reports* **1995**, *21*, 275 – 325.

(5) McKeen, L. W. Polyimides. *Film Properties of Plastics and Elastomers* **2017**, 147–185.

(6) Her, S.-C.; Wang, Y. Temperature effect on microstructure and mechanical properties of aluminum film deposited on glass substrates. *Indian Journal of Engineering Materials Sciences* **2015**, *22*, 268–272.

(7) Mwema, F. M.; Oladijo, O. P.; Akinlabi, S. A.; Akinlabi, E. T. Properties of physically deposited thin aluminium film coatings: A review. *Journal of Alloys and Compounds* **2018**, *747*, 306–323.

(8) Matienzo, L. J.; Egitto, F. D. Polymer oxidation downstream from oxygen microwave plasmas. *Polymer Degradation and Stability* **1992**, *35*, 181–192.

(9) Toth, F.; Rammerstorfer, F. G.; Cordill, M. J.; Fischer, F. D. Detailed modelling of delamination buckling of thin films under global tension. *Acta Materialia* **2013**, *61*, 2425–2433.

(10) Macionczyk, F.; Brückner, . W.; Brü, W. Tensile testing of AlCu thin films on polyimide foils. *Journal of Vacuum Science and Technology B: Microelectronics and Nanometer Structures Processing* **1999**, *86*, 4922–4929.

(11) Trost, C. O. W.; Lassnig, A.; Kreiml, P.; Jörg, T.; Terziyska, V. L.; Mitterer, C.; Cordill, M. J. Enthalpy-Driven Self-Healing in Thin Metallic Films on Flexible Substrates. *Advanced Materials* **2024**, *36*, 2401007.

(12) Li, T.; Huang, Z. Y.; Xi, Z. C.; Lacour, S. P.; Wagner, S.; Suo, Z. Delocalizing strain in a thin metal film on a polymer substrate. *Mechanics of Materials* **2005**, *37*, 261–273.

(13) Katnani, A. D.; Knoll, A.; Mycek, M. A. Effects of environment and heat treatment on an oxygen plasma-treated polyimide surface and its adhesion to a chromium overcoat. *Journal of Adhesion Science and Technology* **1989**, *3*, 441–453.

(14) Lassnig, A.; Terziyska, V. L.; Zalesak, J.; Jörg, T.; Toebbens, D. M.; Griesser, T.; Mitterer, C.; Pippan, R.; Cordill, M. J. Microstructural Effects on the Interfacial Adhesion of Nanometer-Thick Cu Films on Glass Substrates: Implications for Microelectronic Devices. *ACS Applied Nano Materials* **2020**, *4*, 61 – 70.

(15) Lu, N.; Wang, X.; Suo, Z.; Vlassak, J. Metal films on polymer substrates stretched beyond 50%. *Applied Physics Letters* **2007**, *91*, 221909.

(16) Marx, V. M.; Toth, F.; Wiesinger, A.; Berger, J.; Kirchlechner, C.; Cordill, M. J.; Fischer, F. D.; Rammerstorfer, F. G.; Dehm, G. The influence of a brittle Cr interlayer on the deformation behavior of thin Cu films on flexible substrates: Experiment and model. *Acta Materialia* **2015**, *89*, 278.

(17) Putz, B.; Schoeppner, R. L.; Glushko, O.; Bahr, D. F.; Cordill, M. J. Improved electromechanical performance of gold films on polyimide without adhesion layers. *Scripta Materialia* **2015**, *102*, 23–26.

(18) Oh, S. H.; Rentenberger, C.; Im, J.; Motz, C.; Kiener, D.; Karnthaler, H. P.; Dehm, G. Dislocation plasticity of Al film on polyimide investigated by cross-sectional in situ transmission electron microscopy straining. *Scripta Materialia* **2011**, *65*, 456–459.

(19) Putz, B.; Milassin, G.; Butenko, Y. V.; Voelker, B.; Gammer, C.; Semprimoschnig, C. O. A.; Cordill, M. J. Combined TEM and XPS studies of metal - polymer interfaces for space applications. *Surface & Coatings Technology* **2017**, *332*, 368–375.

(20) Atanasoska, L.; Anderson, S. G. H.; Meyer, H. M.; Weaver, J. H. XPS study of chemical bonding at polyimide interfaces with metal and semiconductor overlayers. *Vacuum* **1990**, *40*, 85–90.

(21) Putz, B.; Milassin, G.; Butenko, Y. V.; Voelker, B.; Gammer, C.; Semprimoschnig, C. O. A.; Cordill, M. J. Interfacial mutations in the Al-polyimide system. *Surface and Interface Analysis* **2018**, *50*, 579 – 586.

(22) Putz, B.; Wurster, S.; Edwards, T. E.; Voelker, B.; Milassin, G.; Toebbens, D. M.; Semprimoschnig, C. O. A.; Cordill, M. J. Mechanical and optical degradation of flexible optical solar reflectors during simulated low earth orbit thermal cycling. *Acta Astronautica* **2020**, *175*, 277–289.

(23) Du, Y. K.; Gardella, J. A. J. A study of the interaction between thermally deposited aluminum films and fluoropolymer substrates. *Journal of Vacuum Science and Technology* **1995**, *13*, 1907–1912.

(24) Vasile, M. J.; Bachman, B. J. Aluminum deposition on polyimides: The effect of in-situ ion bombardment. *Journal of Vacuum Science and Technology A* **1989**, *7*, 2992–2997.

(25) Jen, S.; Bertrand, J. A.; George, S. M. Critical tensile and compressive strains for cracking of Al2O3 films grown by atomic layer deposition. *Journal of Applied Physics* **2011**, *109*, 084305.

(26) Gramatte, S.; Politano, O.; Cancellieri, C.; Utke, I.; Jeurgens, L. P. H.; Turlo, V. Effect of hydrogen on the local chemical bonding states and structure of amorphous alumina by atomistic and electrostatic modeling of Auger parameter shifts. *arXiv:2408.08255 [cond-mat.mtrl-sci]* **submitted 15-08-2024, accessed 03-03-2025**,

(27) Edwards, T. E.; Xie, T.; della Ventura, N. M.; Casari, D.; Guerra, C.; Huszar, E.; Maeder, X.; Schwiedrzik, J. J.; Utke, I.; Pethö, L.; Michler, J. On the thinnest Al2O3 interlayers in Al-based nanolaminates to enhance strength, and the role of constraint. *Acta Materialia* **2022**, 118345.

(28) Putz, B.; Edwards, T. E.; Huszar, E.; Pethö, L.; Kreiml, P.; Cordill, M. J.; Thiaudiere, D.; Chiroli, S.; Zighem, F.; Faurie, D.; Renault, P. O.; Michler, J. In situ fragmentation of Al/Al2O3 multilayers on flexible substrates in biaxial tension. *Materials and Design* **2023**, *232*, 112081.

(29) Putz, B.; Edwards, T. E.; Huszar, E.; Gruber, P. A.; Gradwohl, K.-P.; Kreiml, P.; Többens, D. M.; Michler, J. Electromechanical Behavior of Al/Al2O3 Multilayers on Flexible Substrates: Insights from In Situ Film Stress and Resistance Measurements. *Advanced Engineering Materials* **2022**, *25*, 2200951.

(30) Gruber, P. A.; Böhm, J.; Onuseit, F.; Wanner, A.; Spolenak, R.; Arzt, E. Size effects on yield strength and strain hardening for ultra-thin Cu films with and without passivation: A study by synchrotron and bulge test techniques. *Acta Materialia* **2008**, *56*, 2318–2335.

(31) Husain, S. A.; Kreiml, P.; Renault, P.-O.; Mitterer, C.; Cordill, M. J.; Faurie, D. Link between cracking mechanisms of trilayer films on flexible substrates and electromechanical reliability under biaxial loading. *Journal of Vacuum Science and Technology A* **2023**, *41*, 033403.

(32) Cordill, M.; Fischer, F.; Rammerstorfer, F.; Dehm, G. Adhesion energies of Cr thin

films on polyimide determined from buckling: Experiment and model. *Acta Materialia* **2010**, *58*, 5520–5531.

(33) Putz, B.; Milassin, G.; Butenko, Y.; Voelker, B.; Gammer, C.; Semprimoschnig, C.; Cordill, M. J. Combined TEM and XPS studies of metal - polymer interfaces for space applications. *Surface and Coatings Technology* **2017**, *332*, 368–375.

(34) Valdesueiro, D.; Meesters, G. M.; Kreutzer, M. T.; van Ommen, J. R. Gas-phase deposition of ultrathin aluminium oxide films on nanoparticles at ambient conditions. *Materials* **2015**, *8*, 1249–1263.

(35) Sun, Y.; Padbury, R. P.; Akyildiz, H. I.; Goertz, M. P.; Palmer, J. A.; Jur, J. S. Influence of Subsurface Hybrid Material Growth on the Mechanical Properties of Atomic Layer Deposited Thin Films on Polymers. *Chemical Vapor Deposition* **2013**, *19*, 134–141.

(36) Niemelä, J. P.; Rohbeck, N.; Michler, J.; Utke, I. Molecular layer deposited alucone thin films from long-chain organic precursors: from brittle to ductile mechanical characteristics. *Dalton Transactions* **2020**, *49*, 10832–10838.

(37) Cancellieri, C.; Gramatte, S.; Politano, O.; Lapeyre, L.; Klimashin, F. F.; Maćkosz, K.; Utke, I.; Novotny, Z.; Müller, A.; Vockenhuber, C.; Turlo, V.; Jeurgens, L. P. H. Effect of hydrogen on the chemical state, stoichiometry and density of amorphous Al2O3 films grown by thermal atomic layer deposition. *Surface and Interface Analysis* **2024**, *56*, 293 – 304.

(38) Frank, S.; Handge, U. A.; Olliges, S.; Spolenak, R. The relationship between thin film fragmentation and buckle formation: Synchrotron-based in situ studies and two-dimensional stress analysis. *Acta Materialia* **2009**, *57*, 1442 – 1453, Cited by: 114.

(39) Frank, S.; Gruber, P. A.; Handge, U. A.; Spolenak, R. In situ studies on the cohesive properties of α- and β-Ta layers on polyimide substrates. *Acta Materialia* **2011**, *59*, 5881–5892.

(40) Marx, V. M.; Kirchlechner, C.; Zizak, I.; Cordill, M. J.; Dehm, G. Adhesion measurement of a buried Cr interlayer on polyimide. *Philosophical Magazine* **2015**, *95*, 1982 – 1991.

(41) Noyan, I. C.; Cohen, J. B. *Residual Stress: Measurement by Diffraction and Interpretation*; Springer-Verlag, Pages 15-36, 1987.

(42) Faurie, D.; Zighem, F.; Godard, P.; Parry, G.; Sadat, T.; Thiaudiere, D.; Renault, P. O. In situ x-ray diffraction analysis of 2D crack patterning in thin films. *Acta Materialia* **2019**, *165*, 177–182.

(43) Lu, N.; Wang, X.; Suo, Z.; Vlassak, J. J. Failure by simultaneous grain growth, strain localization, and interface debonding in metal films on polymer substrates. *Journal of Materials Research* **2009**, *24*, 379–385.

(44) Cordill, M. J.; Kreiml, P.; Putz, B.; Mitterer, C.; Thiaudiere, D.; Mocuta, C.; Renault, P. O.; Faurie, D. Role of layer order on the equi-biaxial behavior of Al/Mo bilayers. *Scripta Materialia* **2021**, *194*, 113656.

(45) Blanckenhagen, B. V.; Gumbsch, P.; Arzt, E. Dislocation sources in discrete dislocation simulations of thin-film plasticity and the Hall-Petch relation. *Modelling and Simulation in Materials Science and Engineering* **2001**, *9*, 157–169.

(46) Hall, E. O. The Deformation and Ageing of Mild Steel: III Discussion of Results. *Proceedings of the Physical Society. Section B* **1951**, *64*, 747.

(47) Cordero, Z. C.; Knight, B. E.; Schuh, C. A. Six decades of the Hall–Petch effect – a survey of grain-size strengthening studies on pure metals. *International Materials Reviews* **2016**, *61*, 495 – 512.

(48) Elias, H.; Hyde, D. M. An elementary introduction to stereology (quantitative microscopy). *The American journal of anatomy* **1980**, *159 4*, 412–46.

(49) Nix, W. D. Mechanical properties of thin films. *Metallurgical Transactions A* **1989**, *20*, 2217–2245.

(50) Glushko, O.; Cordill, M. J. Electrical Resistance of Metal Films on Polymer Substrates Under Tension. *Experimental Techniques* **2014**, *40*, 303–310.

(51) Gutnik, D.; Kleinbichler, A.; Imrich, P.; Cordill, M.; Lassnig, A. Adhesion of WTi to polyimide measured by complementary methods. *Surface and Coatings Technology* **2023**, *475*, 130148.

(52) Agrawal, D. C.; Raj, R. Measurement of the ultimate shear strength of a metal-ceramic interface. *Acta Metallurgica* **1989**, *37*, 1265–1270.

(53) Glushko, O.; Putz, B.; Cordill, M. J. Determining effective crack lengths from electrical measurements in polymer-supported thin films. *Thin Solid Films* **2020**, *699*, 137906.

(54) Collaud, M.; Nowak, S. H.; Küttel, O. M.; Gröning, P.; Schlapbach, L. Surface modifications of polypropylene after in-situ Ar and N2 plasma treatments: an XPS study. *Applied Surface Science* **1993**, *72*, 19–29.

(55) Lee, S.-Y.; Park, K. R.; Kang, S.-G.; Lee, J.; Jeon, E.-C.; Shim, C.-H.; pyoung Ahn, J.; Kim, D.-I.; Han, H. N.; Joo, Y.; Kim, C.; Choi, I.-S. Selective crack suppression during deformation in metal films on polymer substrates using electron beam irradiation. *Nature Communications* **2019**, *10*, 4454.

(56) Xomalis, A.; Hain, C.; Groetsch, A.; Klimashin, F. F.; Nelis, T.; Michler, J.; Schwiedrzik, J. J. Resist-Free E-beam Lithography for Patterning Nanoscale Thick Films on Flexible Substrates. *ACS Applied Nano Materials* **2023**, 3388–3394.

(57) Jang, S.; Kim, Y. A.; Lim, B.; Cho, S. M. Enhancement of peel strength between Cu and polyimide film by introduction of 4,4-bipyridine monomolecular layer. *Surfaces and Interfaces* **2025**, 106444.

(58) Higgs, D. J.; Dumont, J.; Sharma, K.; George, S. M. Spatial molecular layer deposition of polyamide thin films on flexible polymer substrates using a rotating cylinder reactor. *Journal of Vacuum Science and Technology* **2018**, *36*, 01117.

(59) Azpitarte, I.; Botta, G. A.; Tollan, C.; Knez, M. SCIP: a new simultaneous vapor phase coating and infiltration process for tougher and UV-resistant polymer fibers. *RSC Advances* **2020**, *10*, 15976 – 15982.

(60) Guo, H. C.; Ye, E.; Li, Z.; Han, M.; Loh, X. J. Recent progress of atomic layer deposition on polymeric materials. *Materials science & engineering. C, Materials for biological applications* **2016**, *70 Pt 2*, 1182–1191.

(61) Spagnola, J. C.; Gong, B.; Arvidson, S. A.; Jur, J. S.; Khan, S. A.; Parsons, G. N. Surface and sub-surface reactions during low temperature aluminium oxide atomic layer deposition on fiber-forming polymers. *Journal of Materials Chemistry* **2010**, *20*, 4213–4222.

(62) Edwards, T. E. J.; Xie, T.; della Ventura, N. M.; Casari, D.; Guerra, C.; Huszár, E.; Maeder, X.; Schwiedrzik, J. J.; Utke, I.; Pethö, L.; Michler, J. On the thinnest Al2O3 interlayers in Al-based nanolaminates to enhance strength, and the role of constraint. *Acta Materialia* **2022**, *240*, 118345.

(63) Matoy, K.; Schönherr, H.; Detzel, T.; Schöberl, T.; Pippan, R.; Motz, C.; Dehm, G. A comparative micro-cantilever study of the mechanical behavior of silicon based passivation films. *Thin Solid Films* **2009**, *518*, 247–256.

(64) Kääriäinen, T.; Cameron, D. C. Plasma-Assisted Atomic Layer Deposition of Al 2 O 3 at Room Temperature. *Plasma Processes and Polymers* **2009**,

(65) Djaziri, S.; Thiaudière, D.; Geandier, G.; Renault, P. O.; Bourhis, E. L.; Goudeau, P.; Castelnau, O.; Faurie, D. Controlled biaxial deformation of nanostructured W/Cu thin

films studied by X-ray diffraction. *Surface and Coatings Technology* **2010**, *205*, 1420–1425.

(66) Jansen, H. C.; Sharma, A.; Wieczerzak, K.; Nayak, G. K.; Schneider, J. M.; Schwiedrzik, J. J.; Edwards, T. E.; Michler, J. On the efficacy of Xe+-pFIB preparation to avoid Ga+-FIB induced phase transformations in Al-Ni alloys. *Scripta Materialia* **2025**,

(67) Geandier, G.; Thiaudiere, D.; Randriamazaoro, R. N.; Chiron, R.; Djaziri, S.; Lamongie, B.; Diot, Y.; Bourhis, E. L.; Renault, P. O.; Goudeau, P.; Bouaffad, A.; Castelnau, O.; Faurie, D.; Hild, F. Development of a synchrotron biaxial tensile device for in situ characterization of thin films mechanical response. *Rev. Sci. Instrum* **2010**, *81*, 103903.

(68) Toebbens, D. KMC-2: an X-ray beamline with dedicated diffraction and XAS endstations at BESSY II. *J. Large-Scale Res. Facil.* **2016**, *2*, 1.

(69) Djaziri, S.; Faurie, D.; Renault, P. O.; Bourhis, E. L.; Goudeau, P.; Geandier, G.; Thiaudiere, D. Yield surface of polycrystalline thin films as revealed by non-equibiaxial loadings at small deformation. *Acta Materialia* **2013**, *61*, 5067–5077.

(70) Wern, H.; Koch, N.; Maas, T. Self-Consistent Calculation of the X-Ray Elastic Constants of Polycrystalline Materials for Arbitrary Crystal Symmetry. Residual Stresses VI, ECRS6. 2002; pp 127–132.

TOC Graphic

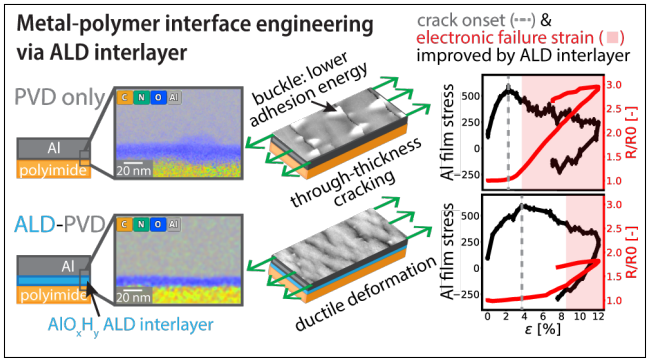
Metal-polymer interface engineering
via ALD interlayer
crack onset (---) &
electronic failure strain (■)
improved by ALD interlayer
PVD only
Al
polyimide
20 nm
buckle: lower
adhesion energy
through-thickness
cracking
ALD-PVD
Al
polyimide
20 nm
AlOxHy ALD interlayer
ductile deformation
Al film stress
R/R0 [-]
ε [%]